INSTITUTE OF PHYSICS PUBLISHING JOURNAL OF PHYSICS B: ATOMIC, MOLECULAR AND OPTICAL PHYSICS

J. Phys. B: At. Mol. Opt. Phys. **39** (2006) 4097–4111 doi:10.1088/0953-4075/39/20/008

Single ionization of helium by 102 eV electron impact: three-dimensional images for electron emission

M Dürr[1], C Dimopoulou[1], A Dorn[1], B Najjari[1], I Bray[2], D V Fursa[2], Zhangjin Chen[3], D H Madison[3], K Bartschat[4] and J Ullrich[1]

[1] Max-Planck-Institut für Kernphysik, Saupfercheckweg 1, 69117 Heidelberg, Germany
[2] ARC Centre for Antimatter-Matter Studies, Murdoch University, Perth, WA 6150, Australia
[3] Laboratory of Atomic and Molecular Research, University of Missouri-Rolla, Rolla, MO 65409, USA
[4] Department of Physics and Astronomy, Drake University, Des Moines, IA 50311, USA

E-mail: Alexander.Dorn@mpi-hd.mpg.de

Received 18 July 2006, in final form 28 July 2006
Published 2 October 2006
Online at stacks.iop.org/JPhysB/39/4097

Abstract

Single ionization of helium by 102 eV electron impact has been studied by measuring the momentum vectors of all final-state particles, i.e., two electrons and the He^+ ion, with an advanced reaction microscope. Fully differential cross sections for asymmetric scattering geometry, which have been normalized to an absolute scale, have been obtained covering a large range of emission angles for the emitted low-energy ($E \leqslant 15$ eV) electron and different scattering angles for the fast electron. Strong electron emission out of the projectile scattering plane is confirmed for electron impact, as was observed before for heavy-ion impact ionization. The data are compared with theoretical predictions from a three-Coulomb wavefunction model, first-order and second-order distorted-wave approaches, as well as a convergent close-coupling calculation.

1. Introduction

Fundamental atomic reactions, such as electron impact-induced single ionization of atoms and molecules, play a key role in various fields, e.g., quantum chemistry, radiation damage and solid-state phenomena. Furthermore, because the Coulomb and spin-dependent interactions among the particles are exactly known, they are benchmark systems for our understanding of correlated dynamical few-body processes. Experimentally, these collisions can be studied in great detail, since the number of participating particles is easily controlled and kinematically complete experiments can be performed. The so-called (e, 2e) experiments, where the momentum vectors of all final-state particles are determined, have been studied for a long time beginning with the pioneering work of Ehrhardt's group more than 35 years ago [1] (for a review, see [2]). Theoretically, tremendous progress has been achieved in recent

years in describing the collision dynamics. Among the most sophisticated approximate models are those employing analytical three-body continuum wavefunctions [3–5], such as the three-Coulomb wavefunction (3C) [6], as well as distorted-wave approaches, which treat the projectile–target interaction up to second order (e.g. [7–11]). Impressive progress has also been made in forming numerical solutions of the full three-body Coulomb system based on non-perturbative approaches, such as exterior complex scaling (ECS) [12], convergent close-coupling (CCC) [13] and time-dependent close-coupling (TDCC) [14]. While the ECS method was only recently applied to describe electron-impact single ionization of helium within a full four-body description of the system [15, 16], several calculations describing (e, 2e) impact on helium within the CCC formalism have been published [17–19]. For helium, the CCC approach often reduces the four-body system to an effective three-body problem through a frozen-core model with one electron always occupying the 1s orbital of He^+, and good agreement with presently available (e, 2e) data from low to high impact energies has been obtained. Most recently, the TDCC method has also been applied to fully differential ionization of helium by low-energy electrons [20].

So far, the above numerically elaborate approaches were tested predominantly in the so-called coplanar scattering geometry, where the ionized electron with the momentum $\boldsymbol{k}_2$ is ejected into the scattering plane determined by the incoming and scattered projectile momentum vectors $\boldsymbol{k}_0$ and $\boldsymbol{k}_1$, respectively. However, this might not be a sufficient test of theory, as was demonstrated impressively by Schulz *et al* [21] in a recent kinematically complete experiment for fast ion-impact (100 MeV/u C^{6+}) ionization of helium. In this work, the full 3D emission pattern of a slow ($E = 6.5$ eV) ionized electron was measured for the first time. The experiment was performed in the perturbative regime at small energy and momentum transfer, at a projectile speed of $v_P = 60$ (atomic units are used unless otherwise stated) and a projectile charge of $Z_P = 6$. Thus, the perturbation parameter $Z_P/v_P = 0.1$ was small, i.e., perturbative methods were generally expected to do well. The experimental cross sections, however, revealed an unexpected strong electron emission out of the scattering plane, which could not be reproduced by state-of-the-art continuum distorted-wave calculations. The latter calculations, on the other hand, were in good agreement with experiment in the scattering plane. While experimental evidence was provided that the problem stems from the projectile scattering from the target nucleus [22], no quantitative theoretical description has yet emerged [23–25] that can reproduce the experimental data. In fact, the work of Schulz *et al* was recently criticized [26], suggesting that the observed electron emission out of the scattering plane was an instrumental effect, due to an insufficient resolution of the momentum transfer.

The recent development of an advanced reaction microscope now allows us to record high-resolution 3D images for electron-impact ionization, i.e., to provide fully differential cross sections (FDCS) for almost all directions of low-energy electron emission ($E \leqslant 15$ eV) in an (e, 2e) experiment. The resolution of the momentum transfer is better by a factor of 2 to 3 compared to that in the ion-impact experiments reported by Fischer *et al* [27]. Therefore, it is now possible to examine whether strong electron emission out of the scattering plane is present for electron-impact ionization as well and to check the extracted cross sections for resolution effects. In a recent publication [28] we presented the 3D emission patterns for two kinematical cases, one of which, with small perturbation parameter $Z_P/v_P = 0.12$ at a projectile energy of $E_0 = 1$ keV, came close to the collision kinematics of the ion-impact experiment performed by Schulz *et al* [21]. In this case, out-of-plane emission was observed as well, although with lower relative intensity compared to the ion-impact data.

In the second case, at a reduced projectile energy of $E_0 = 102$ eV, a strongly increased out-of-plane emission compared to the 1 keV data was observed. To date, no systematic study of the 3D emission patterns has been performed to test the quality of the state-of-the-art theoretical

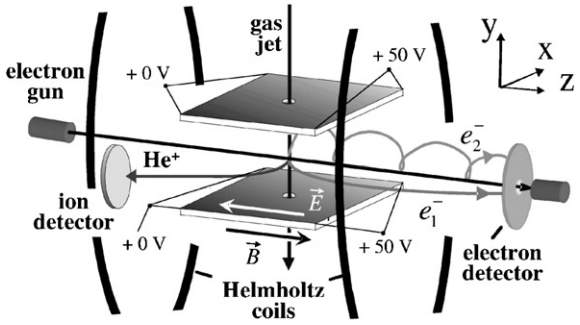

Figure 1. Scheme of the experimental set-up.

models mentioned above. Therefore, in this paper we present a comprehensive set of 3D cross sections for $E_0 = 102$ eV for several projectile scattering angles and energies of the emitted slow electron. We compare these data with the predictions obtained by several sophisticated theories: the three-Coulomb wavefunction approach (3C), a first-order and two second-order distorted-wave Born methods (DWB1 and DWB2, respectively) and the convergent-close coupling (CCC) approach.

No previous experiments for electron-impact ionization covered a large fraction of the full solid angle for electron emission, and even studies of any non-coplanar geometries are scarce; see Röder *et al* [29] for one example. Most of the existing out-of-plane experiments investigating the ionization dynamics were performed for equal energy-sharing conditions and in particular geometries, e.g., with both final-state electrons being emitted perpendicular to the incoming beam direction, thereby implying relatively large energy and momentum transfers [30–33]. For low-energy electron emission at small momentum transfer, to the best of our knowledge, only Beaty *et al* [34] examined the shapes of the so-called binary and recoil lobes in a particular non-coplanar geometry. However, they did not find any peculiarity.

On the other hand, a large amount of work has been devoted in the past to fast, impulsive non-coplanar collisions with equal energy sharing in order to find the best conditions for using (e, 2e) experiments as a spectroscopy technique. Deviations from coplanar scattering geometry were small since out-of-plane azimuthal angles below 20°–30° were studied. Typical cross sections are two to three orders of magnitude smaller than for strongly asymmetric energy sharing and do not contribute significantly to the total ionization cross section. In summary, the existing fully differential data for electron-impact ionization are available only in selected cuts revealing small patches of the possible momentum space. This is in contrast to the significant importance of accurately known electron-impact ionization cross sections in the strongly asymmetric energy sharing kinematics, which dominates the total ionization cross section.

This paper is organized as follows. Details of the experimental set-up are given in section 2, followed by a brief description of the various theoretical models employed in section 3. The experimental and theoretical results are presented and discussed in section 4, followed by concluding remarks.

2. Experiment

The experiment was performed at the MPI for Nuclear Physics in Heidelberg using a multi-electron recoil-ion momentum spectrometer also known as reaction microscope [35] (figure 1). A well-focused (1 mm), pulsed electron beam (pulse length ≈ 1–2 ns, repetition rate =

200 kHz, $\approx 10^4$ electrons/pulse), produced by a standard thermocathode gun, crosses and ionizes a supersonic He jet (2 mm diameter, 10^{12} atoms cm^{-3}). All three final-state particles, i.e., the scattered projectile electron, the emitted target electron, and the recoiling He^+ ion, were extracted into the opposite directions, respectively, along the projectile beam axis (the longitudinal direction defines the z-axis) by a weak homogeneous electric field (typically 1 V cm^{-1}) over 11 cm and projected onto two-dimensional position-sensitive multi-hit detectors. A uniform longitudinal magnetic field of 6 G was applied to confine the transverse motion of the electrons, such that all electrons with $E_2 \leqslant 15$ eV were collected with the full solid angle. While the ion-detector is equipped with a wedge and strip anode, the electron detector employs a delay-line anode [36] for position read-out with increased multi-hit capability. In this way, a large part of the full solid angle is covered, essentially 100% for the detection of target ions and 80% for electrons below 15 eV. From the hitting positions and the time-of-flight the vector momenta of the particles can be calculated.

Different from all previous designs reported in [35] and [37], the reaction microscope dedicated to electron-impact ionization experiments was decisively improved with the advantage of reaching (i) maximum flexibility in the choice of the electron beam energy and extraction field strengths, (ii) additional redundancy in the data, and (iii) substantially improved resolution for the scattered projectile momentum. This was achieved by guiding the electron projectile beam exactly parallel to the electric and magnetic extraction fields, into the target, and further on to the forward electron detector enabling the detection of the scattered projectiles. The momentum transfer is obtained directly from the scattered electron position and the time-of-flight. Therefore, the resolution for the momentum transfer does not depend on the target gas temperature and is a factor of 2 to 3 better compared to conventional reaction microscopes, where the scattering angle of the projectile is reconstructed from the recoil-ion and the ejected-electron momentum vectors [35]. In order to avoid the complete saturation of the electron detector by the unscattered projectiles ($\approx 10^8$ s^{-1}), a central bore (5 mm diameter) in the MCP stack is required to allow for their passage (see figure 1). In this way, unscattered electrons are collected on the delay-line behind the bore of the detector and degradation of the sensitive detector plates as well as high background due to back-scattering is avoided.

For the data presented in this paper, the scattered projectile electrons were detected together with ejected electrons with transverse momenta in the range $0.2 \leqslant k_\perp \leqslant 1.2$,[5] as well as with the residual ion, such that the triple coincidence of all final-state continuum particles delivered superior background suppression. For the present experiments, as for typical ion-impact data, the recoil-ion momentum resolution perpendicular and parallel to the spectrometer axis was $(\Delta k_\perp, \Delta k_\parallel) \approx (0.25, 0.15)$. The electron momentum resolution depends on how well the time and position of the ionizing collision can be determined and therefore from the temporal pulse-width and the focus diameter of the projectile beam in the target. For the focus diameter of 1 mm and the pulse length of 1.5 ns the transversal momentum resolution of the electrons is better than $\Delta k_\perp \leqslant 0.1$. The longitudinal resolution for the slow ionized electrons is better than $\Delta k_\parallel \leqslant 0.02$, while for the scattered projectiles at $E_0 = 102$ eV $\Delta k_\parallel \leqslant 0.08$. Consequently, the change of the internal energy of the target (the Q-value of the reaction) can also be determined with significantly improved resolution. Thus, processes leaving the He^+ ion in different excited states with principal quantum numbers $n = 1, n = 2$ or $n \geqslant 3$, respectively, can be distinguished. In previous ion-impact FDCS measurements, where the momentum of the scattered projectile remained undetected, this

[5] For reasons of convenience the momentum vector is expressed in cylindrical coordinates: $k_\parallel = k_z, k_\perp = \sqrt{k_x^2 + k_y^2}, \phi = \arctan(k_x/k_y)$.

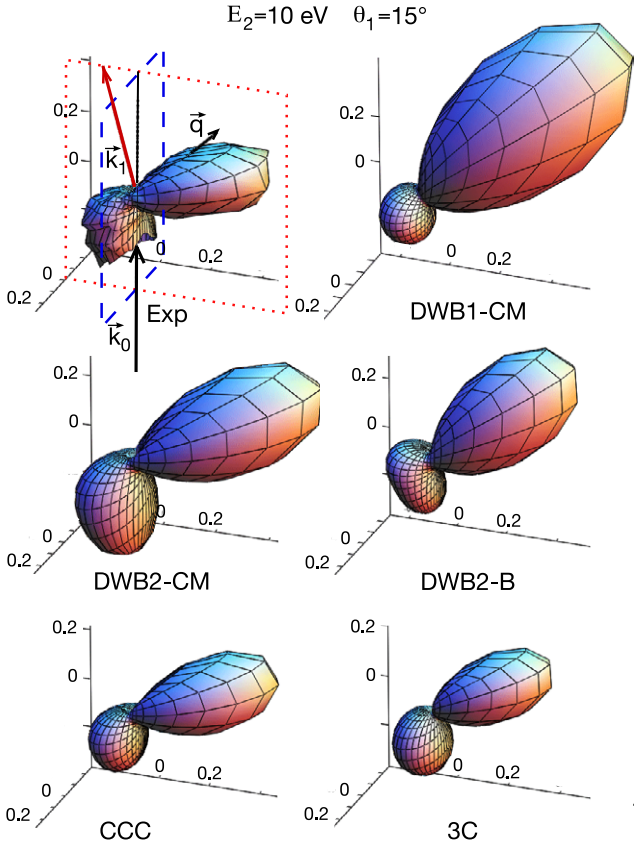

Figure 2. Fully differential cross sections for slow-electron emission ($E_2 = 10$ eV) from single ionization of He by 102 eV electron impact at a fixed deflection angle of $\theta_1 = 15°$. The shapes of the FDCS are plotted as a function of the angle of the emitted electron $d\Omega_2$ with respect to the incoming projectile beam direction. Top row: experiment and DWB1-CM. Middle row: DWB2-CM and DWB2-B theories. Third row: CCC and 3C theories. The cuts in the panel with the experimental data indicate the co-planar geometry (dotted lines) and the perpendicular geometry (dashed lines).

information on the final state of the He^+ ion was not available, i.e., the measured cross sections were summed over all final ionic states.

The parallel alignment of the incoming projectile beam and the magnetic field inside the spectrometer enables a fairly large range of projectile energies to be used, by exploiting the magnetic-lens effect to image a beam focus close to the electron source into the target jet. With the present thermocathode electron gun, beam energies between 30 eV and 2 keV were realized, aiming to reach eV beam energies with meV resolution from a photo-cathode in the near future [38].

For single ionization, the FDCS is commonly expressed as $d^5\sigma/d\Omega_1\, d\Omega_2\, dE_2$, where $d\Omega_1$ and $d\Omega_2$ are the solid angles for the fast and slow outgoing electrons, respectively, and dE_2 denotes the considered energy interval of the slow electron e_2. In the present strongly asymmetric scattering geometry, exchange processes are expected to contribute only weakly, such that the fast outgoing electron is identified as the scattered projectile and the slow electron as the ejected electron. In order to extract the FDCS from the data set obtained with the reaction microscope the scattering angle of the projectile $\theta_1 = \arctan\left(k_{\perp_1}/k_{\parallel_1}\right)$ and the energy of the

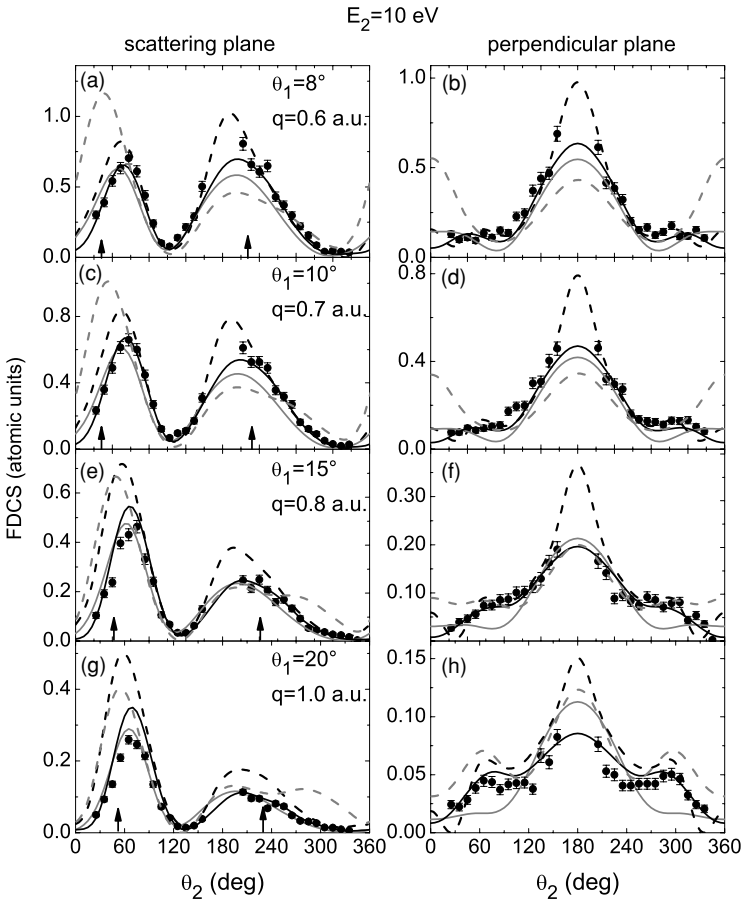

Figure 3. Cuts through the three-dimensional cross section figures as depicted in figure 2 for the scattering plane (left column) and for the perpendicular plane (right column). The FDCS (in atomic units) is plotted as a function of the angle of the emitted electron θ_2 with respect to the incoming projectile beam direction, for a fixed deflection angle of the scattered projectile θ_1 (corresponding to the given momentum transfer $\boldsymbol{q}$) and a fixed emitted electron energy $E_2 = 10$ eV. Theoretical curves: black ——, CCC; grey ——, 3C; black - - -, DWB2-CM; grey - - -, DWB2-B. In the diagrams on the left, the directions of $\boldsymbol{q}$ and $-\boldsymbol{q}$ are marked by arrows.

ejected electron $E_2 = \left(k_{\perp_2}^2 + k_{\parallel_2}^2\right)/2$ are fixed. Since the applied imaging technique covers the full range of azimuthal emission angles for all secondary particles simultaneously, the FDCS can be displayed as a three-dimensional polar plot. An example is given in figure 2. For a more quantitative comparison with theoretical predictions, further cuts in the emission geometry of the ejected electron can be applied. Apart from the intensively studied coplanar geometry, our second choice is a cut through the plane perpendicular to the scattering plane containing the incoming projectile axis, as depicted in the top left panel of figure 2. The cross sections in both, the coplanar and the out-of-plane geometry, are integrated over an angular range of $\pm 10^\circ$ above and below the respective cutting plane. As can be seen in the plots of figures 3 and 4, no experimental data are obtained for near-forward or near-backward electron emission. This is due to the central bore in the electron detector, which does not allow us to detect electrons with transversal momentum component $k_\perp \leqslant 0.2$.

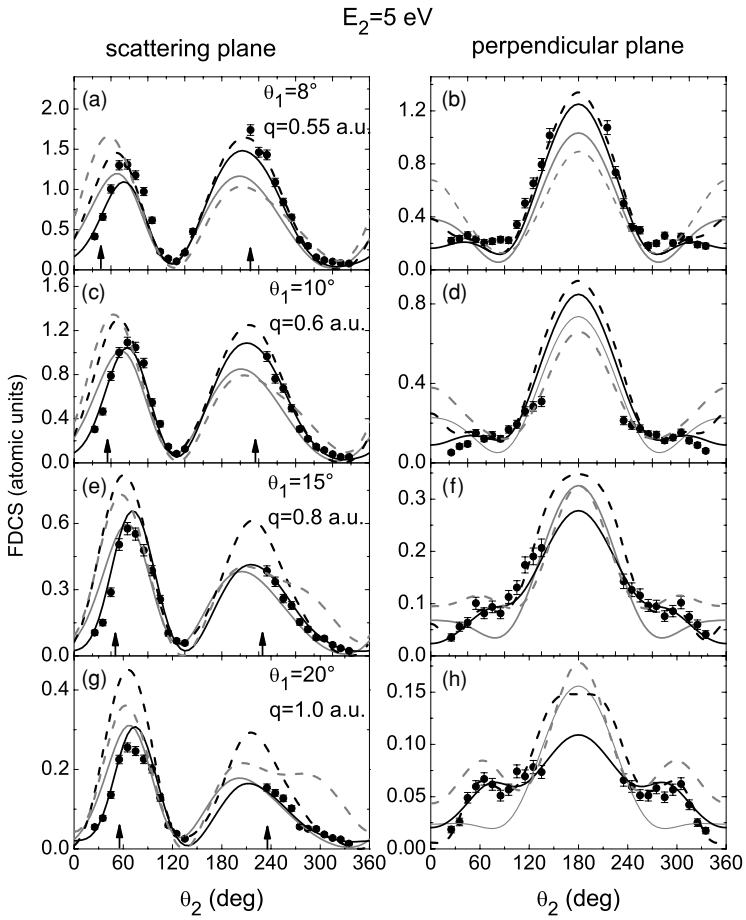

Figure 4. Same as figure 3 for $E_2 = 5$ eV.

The absolute scale of the cross section was not determined directly in the present experiment, but through normalization to a data set measured in coplanar scattering geometry by the Kaiserslautern group. This data set, published in [17][6], is for 100 eV impact energy with a quoted error of 30%. Recall that all data in the present experiment are recorded simultaneously in a single run. Consequently, once the normalization factor has been fixed for one point, the cross sections for all other geometries are inter-normalized across *all* recorded scattering angles and *all* ejected electron energies, thereby providing valuable benchmark data over a wide kinematical range.

3. Theoretical methods

We consider an (e, 2e) collision, in which an incident electron of momentum $\boldsymbol{k}_0$ ionizes a helium target initially at rest in its ground state. Both scattered and ejected electrons are detected with momenta $\boldsymbol{k}_1$ and $\boldsymbol{k}_2$ with respect to the target nucleus[7]. The corresponding fully differential cross section is given by

[6] These data, obtained by J Röder, K Jung and H Ehrhardt, were provided in a private communication.

[7] For a collision with a light projectile and a relatively small momentum transfer, the target nucleus is assumed to have an infinite mass and to be at rest before and after the collision.

$$\frac{\mathrm{d}^6\sigma}{\mathrm{d}\boldsymbol{k}_1\,\mathrm{d}\boldsymbol{k}_2} = \frac{(2\pi)^4}{k_0}|T_{\mathrm{fi}}|^2\delta(E_\mathrm{i} - E_\mathrm{f}). \tag{1}$$

Here E_i and E_f are the total energies of the colliding system before and after the collision, respectively, and T_{fi} denotes the transition amplitude. Although the (e, 2e) process for helium atoms might seem simple due to the small number of particles involved, the problem is difficult because of the long-range nature of the Coulomb interaction. This prevents the particles, even at very large inter-particle distances, from moving freely. Therefore, in the single ionization processes considered here, the asymptotic final state consists of a three-body Coulomb wavefunction and requires particular attention.

3.1. Three-Coulomb wavefunction approach

The three-Coulomb (3C) wavefunction approach was introduced in [6] to describe the ionization process of a hydrogen atom by electron impact and since then has been used extensively in the literature. This approximation is built on a perturbative treatment, but it accounts *asymptotically* for high-order effects in the final state between the two continuum electrons and the residual ion. The T-matrix element T_{fi} in equation (1) is given in the prior form by

$$T_{\mathrm{fi}} = \left\langle \Psi_\mathrm{f}^{(-)} \middle| V_\mathrm{i} \middle| \Phi_\mathrm{i} \right\rangle. \tag{2}$$

Here $|\Phi_\mathrm{i}\rangle$ is the asymptotic initial state of the colliding system. Its spatial part is given by

$$\Phi_\mathrm{i}(\boldsymbol{r}_0, \boldsymbol{r}_1, \boldsymbol{r}_2) = (2\pi)^{-\frac{3}{2}}\,\mathrm{e}^{\mathrm{i}(\boldsymbol{k}_0\cdot\boldsymbol{r}_0)}\phi_\mathrm{He}(\boldsymbol{r}_1, \boldsymbol{r}_2), \tag{3}$$

where $\boldsymbol{r}_0$, $\boldsymbol{r}_1$ and $\boldsymbol{r}_2$ are the position vectors of the incident electron and the two helium electrons with respect to the target nucleus, respectively. Furthermore, $\phi_\mathrm{He}(\boldsymbol{r}_1, \boldsymbol{r}_2)$ represents the ground-state wavefunction of the free helium atom. In the present calculation, it is described by a two-parameter wavefunction (type *d* in [39]).

The interaction potential in the initial state, V_i, is determined from $(\hat{H} - E_\mathrm{i})\Phi_\mathrm{i} = V_\mathrm{i}\Phi_\mathrm{i}$, where $\hat{H}$ is the full Hamiltonian of the system. According to the expression of the initial-state wavefunction determined above, the interaction potential can be written as

$$V_\mathrm{i} = -\frac{2}{|\boldsymbol{r}_0|} + \frac{1}{|\boldsymbol{r}_0 - \boldsymbol{r}_1|} + \frac{1}{|\boldsymbol{r}_0 - \boldsymbol{r}_2|}. \tag{4}$$

The final-state wavefunction, $\Psi_\mathrm{f}^{(-)}$, describing the two electrons in the continuum and the residual bound electron, is represented by a product $\psi_\mathrm{f}^{-}(\boldsymbol{r}_\rho, \boldsymbol{r}_\mu, \boldsymbol{r}_\nu) = \psi_\mathrm{3C}(\boldsymbol{r}_\rho, \boldsymbol{r}_\mu)\phi_{\mathrm{He}^+}(\boldsymbol{r}_\nu)$ with $\rho \neq \mu \neq \nu = 0, 1$ or 2. The 3C wavefunction obeying incoming wave boundary conditions is given by

$$\psi_\mathrm{3C}(\boldsymbol{r}_\rho, \boldsymbol{r}_\mu) = (2\pi)^{-3}\,\mathrm{e}^{\mathrm{i}(\boldsymbol{k}_1\cdot\boldsymbol{r}_\rho + \boldsymbol{k}_2\cdot\boldsymbol{r}_\mu)} C\left(\frac{-1}{k_1}, \boldsymbol{k}_1|\boldsymbol{r}_\rho\right) C\left(\frac{-1}{k_2}, \boldsymbol{k}_2|\boldsymbol{r}_\mu\right) C\left(\frac{1}{2k_{12}}, \boldsymbol{k}_{12}|\boldsymbol{r}_{\rho\mu}\right). \tag{5}$$

Here $\boldsymbol{r}_{12} \equiv \boldsymbol{r}_1 - \boldsymbol{r}_2$ is the relative coordinate between the two outgoing electrons, $\boldsymbol{k}_{12} \equiv (\boldsymbol{k}_1 - \boldsymbol{k}_2)/2$, and $C(\alpha, \boldsymbol{v}|\boldsymbol{r})$ is the pure Coulomb distortion solution of

$$\left(\Delta + 2\mathrm{i}\boldsymbol{v}\cdot\nabla - \frac{2\alpha v}{r}\right) C(\alpha, \boldsymbol{v}|\boldsymbol{r}) = 0. \tag{6}$$

It can be written as $C(\alpha, \boldsymbol{v}|\boldsymbol{r}) = \mathrm{e}^{-\frac{\pi}{2}\alpha}\Gamma(1 - \mathrm{i}\alpha)_1F_1(\mathrm{i}\alpha, 1, -\mathrm{i}vr - \mathrm{i}\boldsymbol{v}\cdot\boldsymbol{r})$.

Finally, we have performed calculations with and without taking into account exchange between the two final state continuum electrons and found it to be unimportant in the present asymmetric energy sharing kinematics. For the 3C calculations shown here exchange is not included.

3.2. Distorted-wave models

In the distorted-wave (DW) models discussed below, it is more convenient to express the T-matrix element $T_{\rm fi}$ of equation (1) in the post form

$$T_{\rm fi} = \langle \Phi_{\rm f}^- | \tilde{V}_{\rm f} | \Psi_{\rm i}^+ \rangle. \tag{7}$$

In the DW approximation, the approximate final-state wavefunction $\Phi_{\rm f}^-$ is expressed as a product of a target wavefunction times a final-state distorted wave $\chi_{\rm f}^-$ for the projectile, i.e.,

$$\Phi_{\rm f}^-(\boldsymbol{r}_0, \boldsymbol{r}_1, \boldsymbol{r}_2) = \phi_{\rm f}^-(\boldsymbol{r}_1, \boldsymbol{r}_2)\chi_{\rm f}^-(\boldsymbol{r}_0). \tag{8}$$

Here $\phi_{\rm f}^-(\boldsymbol{r}_1, \boldsymbol{r}_2)$ is the final target wavefunction. In its simplest form, this wavefunction is expressed as a symmetrized product of the He^+ wavefunction $\varphi_{\rm f}$ for the bound electron times a distorted wave $\chi_{\rm e}^-$ for the ejected electron, i.e.,

$$\phi_{\rm f}^-(\boldsymbol{r}_1, \boldsymbol{r}_2) = 2^{-1/2}[\varphi_{\rm f}(\boldsymbol{r}_1)\chi_{\rm e}^-(\boldsymbol{r}_2) + \varphi_{\rm f}(\boldsymbol{r}_2)\chi_{\rm e}^-(\boldsymbol{r}_1)]. \tag{9}$$

Alternatively, the ejected-electron–residual-ion interaction can be represented by a convergent close-coupling (CCC) or R-matrix with pseudo-states (RMPS) expansion. As shown by Kheifets *et al* [40] for the more complicated simultaneous ionization–excitation process, such expansions make it possible to get effectively converged results for the scattering of the slow ejected electron from the residual He^+ ion, while still treating the projectile–target interaction perturbatively.

By using a Lippmann–Schwinger solution, the exact initial-state wavefunction $\Psi_{\rm i}^+$ can be written as

$$\Psi_{\rm i}^+ = \Phi_{\rm i}^+ + G^+\tilde{V}_{\rm i}\Phi_{\rm i}^+, \tag{10}$$

where $\Phi_{\rm i}^+$ is an initial-state wavefunction as in equation (3), except that the initial-state plane wave for the projectile is replaced by an initial-state projectile distorted wave $\chi_{\rm i}^+$, i.e.,

$$\Phi_{\rm i}^+(\boldsymbol{r}_0, \boldsymbol{r}_1, \boldsymbol{r}_2) = \chi_{\rm i}^+(\boldsymbol{r}_0)\phi_{\rm He}(\boldsymbol{r}_1, \boldsymbol{r}_2). \tag{11}$$

The modified interaction potential $\tilde{V}_{\rm f}$ in (7) is given by

$$\tilde{V}_j = V_{\rm i} - U_j, \qquad j = \text{i or f}. \tag{12}$$

Here $U_{\rm f}$ is the distorting potential used to obtain the distorted wave $\chi_{\rm f}^-$ for the projectile in the final state and $U_{\rm i}$ is the distorting potential used to calculate the distorted wave $\chi_{\rm i}^+$ in the initial state.

The full Green's function operator G^+ in (10) may be expanded in terms of the free Green's function operator G_0^+ as

$$G^+ = G_0^+ + G_0^+\tilde{V}_{\rm i}G_0^+ + \cdots. \tag{13}$$

Consequently, the exact initial-state wavefunction $\Psi_{\rm i}^+$ can be expressed as

$$\Psi_{\rm i}^+ = \Phi_{\rm i}^+ + G_0^+\tilde{V}_{\rm i}\Phi_{\rm i}^+ + \cdots. \tag{14}$$

Truncating this expression after one term yields the first-order DWB1 approximation and truncating after two terms yields the second-order model DWB2. In the present paper, we present two versions of the latter, one developed by Bartschat and co-workers [7–9] and the other developed by Chen and Madison [10, 11]. These methods differ in many aspects, such as the choice of the initial state, the treatment of the ejected-electron–residual-ion interaction, and the evaluation of the second-order term itself. Briefly, Chen and Madison use a single-configuration Hartree–Fock representation of the initial bound state and the single-channel product (9) for the e–He^+ scattering problem of the ejected electron, which neglects exchange between that electron and the remaining 1s electron in He^+. They evaluate the second-order

amplitude without approximation other than representing the complete set of intermediate states by a set of pseudo-states. We will label this approach as DWB2-CM below. On the other hand, the method developed by Bartschat and co-workers (labelled DWB2-B) uses a multi-configuration representation of the initial bound state (the energy of this state in the present calculation is $-2.902\,3320$ Hartree) and treats the e–He^+ problem for the slow ejected electron to numerical accuracy. As a payoff, however, several approximations are made in the evaluation of the second-order term, limiting it to the imaginary part of the Green's function and also applying a closure-type approximation. More details can be found in the references given above.

For the problem at hand, it is not obvious whether the approximations made in the DWB2-CM or DWB2-B models are more severe. Hence, in what follows, we will present results from both models. In order to illustrate the effect of the second-order terms, we also present first-order results obtained by Chen and Madison (DWB1-CM).

3.3. The convergent close-coupling method

The details of the non-perturbative CCC method for electron–helium scattering were given by [41] and then extended to ionization by [42]. Briefly, the target states are written as configuration–interaction (CI) expansions utilizing an orthogonal Laguerre basis. These states are then used to expand the *total* (i.e., including the projectile) e–He wavefunction, and the resulting close-coupling equations are solved in momentum space. The idea is that convergence in the observables of interest should be obtained by just increasing the size of the Laguerre basis. In the case of helium, electron-induced transitions are often dominated by the case where only one electron is excited and the remaining electron is well described by the 1s orbital of He^+. In such cases the frozen-core model, where the CI expansions are restricted to excitation of only one of the electrons, may be applied. On the other hand, when ionization plus excitation processes are significant, as in e–He(2^3S) ionization, more general expansions are required [43].

Upon solution of the close-coupling equations, the CCC method yields amplitudes for excitation of all target states that are energetically accessible. Some of these states are good discrete eigenstates of helium while others are positive-energy pseudostates. Ionization amplitudes are constructed directly from the latter [42].

When applying theory to predict the outcome of an experiment, the goal can be more than just a good reproduction of the experimental data. Once good agreement is achieved, it is often instructive to perform less complete calculations in order to see if there are any specific aspects in the calculation that are more important than others. For the present cases of interest, we found that the frozen-core model and the dropping of exchange between the incoming projectile and the target electrons are very good approximations, i.e., making those approximations (as done in the DW models) hardly changes the final results. The CCC results presented below are from a frozen-core calculation that couples $23-\ell$ singlet states for target orbitals with orbital angular momentum $\ell \leqslant 5$. Note that such calculations are considerably less involved than those for equal energy sharing [19], where exchange is critically important.

4. Results and discussion

Figure 2 exhibits the experimental and theoretical three-dimensional electron emission patterns for single ionization of He by 102 eV electron impact and a scattering angle of $15^\circ \pm 1^\circ$. The energy of the emitted electron is fixed at $E_2 = 10 \pm 1$ eV. In this representation, the FDCS for a particular direction is given as the distance from the origin of the plot to the point on the surface

which is intersected by the ionized electron's trajectory. The cross section patterns are governed by the well-known double-lobe structure, which can be qualitatively understood already within a first-order model: the binary lobe in the direction of $\boldsymbol{q}$ corresponds to electrons emitted in a single binary collision with the projectile, i.e., the target nucleus remains essentially a spectator. For emission along the second lobe, pointing roughly in the direction of $-\boldsymbol{q}$, the target electron initially going along the $\boldsymbol{q}$ direction backscatters in the ionic potential. The ion thus carries a large recoil momentum while the electron is finally emitted into the $-\boldsymbol{q}$ direction, thereby forming the so-called 'recoil lobe'. For a given projectile energy, the ionization process and, therefore, the shapes and relative magnitude of the binary and recoil lobes delicately depend upon the momentum transferred by the projectile, the energy of the emitted electron, and the details of the atomic and ionic potentials. Furthermore, due to the long-range nature of the Coulomb-force, the emitted electron is repelled by the outgoing projectile. The importance of this post-collision interaction (PCI) effect increases with decreasing relative velocity of the two outgoing electrons. For this reason, the binary and recoil lobes do not point exactly along the directions of $\boldsymbol{q}$ and $-\boldsymbol{q}$, respectively. Instead they are tilted away from the outgoing projectile direction. The opposite trend occurs for positive ion impact [44], i.e., in this case the emitted electron is dragged towards the outgoing projectile.

For the present asymmetric kinematics, the angular electron emission pattern has been well studied only in coplanar experiments. The three-dimensional presentation in figure 2 allows for a more complete investigation and reveals new features. First, a significant cross section perpendicular to the projectile scattering plane is observed, thereby bridging the angular range between the binary and recoil lobes. This feature, which was previously observed for ion impact ionization, therefore also exists for electron projectiles. Second, the binary lobe is not axially symmetric. Instead, its slightly flattened shape is consistent with a somewhat suppressed emission along the forward direction.

Also shown in figure 2 are the corresponding cross sections predicted by the DWB1-CM, DWB2-CM, DWB2-B, CCC and 3C methods. From this global comparison of the shapes, the qualitative agreement and the principal shortcomings of the theoretical results can easily be identified. To begin with, the first-order approach is clearly inadequate, yielding too large a ratio between the binary and recoil lobes, a deep minimum separating the two lobes, and a nearly symmetric distribution around the $\pm\boldsymbol{q}$ direction. The DWB2-B calculation improves upon the binary-to-recoil ratio and slightly increases the size of the ring between the two lobes. Overall, however, the second-order effects appear too small in this calculation, particularly regarding the bending of the lobes away from the $\pm\boldsymbol{q}$ directions. The DWB2-CM model, on the other hand, clearly reproduces this bending of the two lobes, in good qualitative agreement with experiment. The same is true for the CCC predictions, which are also in very good agreement with the experimental data. Finally, the 3C approach nicely reproduces the magnitudes and the angular positions of the binary and recoil lobes. Like the DWB1 model, however, it predicts a sharp cross section minimum between the two lobes, in clear contrast to the experiment.

A more quantitative comparison of experiment and theories is shown in figures 3 and 4, where cuts through the three-dimensional cross section patterns are plotted for two different energies of the ejected electron, $E_2 = 10 \pm 1$ eV and 5 ± 1 eV, respectively. For both cases, four different projectile scattering angles, $\theta_1 = 8^\circ$, 10°, $15^\circ(\pm 1^\circ)$ and $20^\circ \pm 2^\circ$, were chosen.

In the left column of the figures, data for emission in the projectile scattering plane are presented, corresponding to a cut through the respective 3D cross sections indicated by the dotted line in the upper left panel of figure 2. The right column, on the other hand, presents data in the plane perpendicular to the scattering plane. This includes the incoming beam direction and is indicated by the dashed line in the upper left corner of figure 2. For both

planes, the cross section is plotted versus the polar angle θ_2 with respect to the projectile beam forward direction. As mentioned above, the absence of experimental data points in a cone of about 25° around the axis of the incoming projectile beam is due to the hole in the electron detector.

The series of cross sections presented allows us to systematically examine the shape and absolute values of the emission pattern. In the scattering plane the binary-to-recoil peak height ratio increases for increasing projectile scattering angle θ_1 or, equivalently, for increasing momentum transfer q. The ratio also increases with increasing ejected electron energy E_2, a behaviour studied in detail earlier (e.g. [45]). Since the angular position of the recoil peak is close to the incoming beam axis, it not only appears in the scattering plane but also in the perpendicular geometry (right columns in figures 3 and 4) as a dominant feature at $\theta_2 = 180°$. In addition, side peaks are visible around 70° and 290°. For both energies, $E_2 =$ 5 eV and 10 eV, they strongly increase in intensity relative to the recoil lobe for increasing scattering angles or momentum transfers, respectively. This observation is consistent with a higher order mechanism being responsible for the side lobes as, e.g., the consecutive scattering of the projectile on the target electron and the target nucleus discussed in [22]. Higher order effects are known to become more important for large momentum transfers, corresponding to small classical impact parameters.

In figures 3 and 4, the experimental FDCS are again compared with predictions from various theoretical models, namely CCC, 3C, DWB2-CM and DWB2-B. For emission in the scattering plane, the 3C calculation systematically underestimates the recoil lobe heights at small q, while the agreement with experiment improves substantially for the largest q studied here. In the perpendicular plane, the 3C model again consistently underestimates the recoil peak close to $\theta_2 = 180°$ for small momentum transfer q. For larger momentum transfers, not only a quantitative disagreement persists but the side peaks at 70° and 290° are completely absent in the 3C results. In contrast, both DWB2 models qualitatively reproduce these structures in the perpendicular plane, with the DWB2-CM approach doing very well also in a quantitative comparison. For emission in the scattering plane, the latter is in good agreement with experiment at small scattering angles, particularly concerning the recoil peak. The binary peak is reproduced, although the width is slightly too large and the peak is shifted by about 10° towards small angles. In the case of larger scattering angles, $\theta_1 = 15°$ and 20°, DWB2-CM significantly overestimates the magnitude of both binary and recoil peaks. Overall, we note substantial differences between the DWB2-CM and DWB2-B results. These suggest a strong sensitivity of these predictions to the details of the models, including the description of the ground state, the ejected-electron–residual-ion interaction, and the evaluation of the second-order term. A more detailed analysis of these differences is beyond the scope of the present work and will be deferred to a future publication. Finally, the CCC calculation at $E_2 = 5$ eV yields very good agreement for essentially all cuts with a small underestimate of the binary peak for $\theta_1 = 8°$. There is also good agreement for most cuts at $E_2 = 10$ eV, with the exception of the results for $\theta_1 = 15°$ and 20°, where the binary peaks lie above experiment by 15% and 25%, respectively.

As suggested already from the inspection of figure 2, the out-of-plane emission is dominated by higher order effects in the projectile–target interaction. To study this in more detail, a further cut through the three-dimensional emission pattern as shown in figure 5(a) is applied, where the cutting plane is perpendicular to the momentum transfer vector $\boldsymbol{q}$. The resulting emission pattern is presented in figure 5(c) for a fixed emitted electron energy of $E_2 = 10$ eV and a scattering angle of $\theta_1 = 15°$. The FDCS in this particular non-coplanar geometry is plotted as a function of the emission angle of the ejected electron θ_2', which is

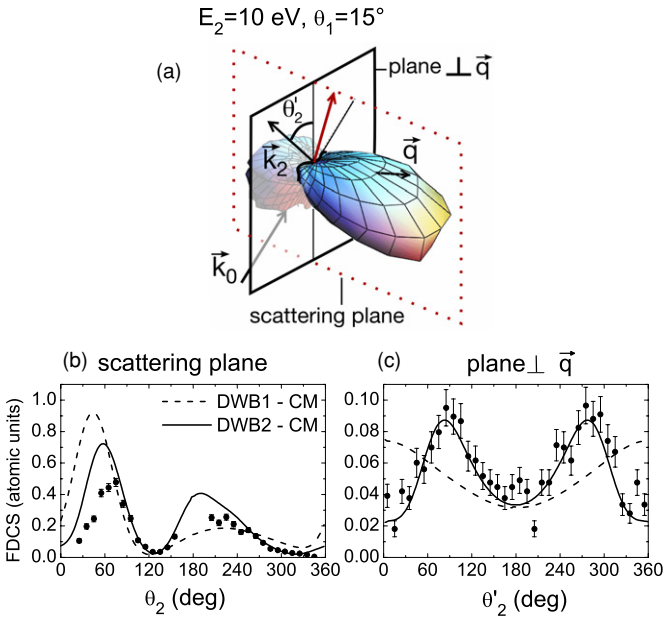

Figure 5. Illustration of the emission plane perpendicular to the momentum transfer vector $\boldsymbol{q}$ (a). DWB1-CM (dashed line) and DWB2-CM (solid line) results for the FDCS in the scattering plane (b) and the plane perpendicular to the momentum transfer $\boldsymbol{q}$ (c) for a fixed emitted electron energy $E_2 = 10$ eV and a scattering angle of 15°.

defined as the angle between its momentum $\boldsymbol{k}_2$ and the scattering plane, where 0° corresponds to 'forward' emission in the scattering plane.

Applying a cut in this particular plane brings along several advantages. Firstly, the full range of emission angles from 0° to 360° is accessible in the experiment. Secondly, the fine details of higher order projectile–target interaction can be studied in the plane perpendicular to $\boldsymbol{q}$, where the contributions of the binary and recoil lobes are small. Correspondingly the cross section is by a factor of 10 lower compared to that inside the scattering plane. In the experimental non-coplanar cross section two maxima are observed at around $\theta_2' = 90°$ and $\theta_2' = 270°$, that is for electron emission perpendicular to the scattering plane. A very similar behaviour of the cross section has been found for electron and ion impact at high energies for emission in the plane perpendicular to $\boldsymbol{q}$ [28] . For ion-impact these contributions have been traced back to higher order interaction between the projectile and the target nucleus [22]. The importance of higher order projectile–target interaction is demonstrated in figures 5(b) and (c), where the first- and second-order results obtained in the DWB1-CM and DWB2-CM models are plotted for the coplanar geometry and the plane perpendicular to the momentum transfer $\boldsymbol{q}$, respectively. Both models are able to qualitatively predict the in-plane results, with some improvement over the first-order results achieved by the second-order treatment. For emission in the plane perpendicular to $\boldsymbol{q}$, however, the second-order model yields excellent agreement with experiment, while the first-order results exhibit a qualitatively incorrect angular distribution. Since the DWB1-CM calculation accounts for the projectile–nucleus interaction in the incident and final channel, the observed maxima in the non-coplanar geometry cannot be uniquely traced back the projectile–nucleus scattering. The fact that the second-order calculation DWB2-CM provides a better description in this particular plane, indicates the

strongly correlated three-body dynamics at the low projectile velocity chosen in the present experiment.

5. Conclusions

We have performed a systematic study of the three-dimensional electron emission pattern for single ionization of helium by 102 eV electron impact. In addition to the well-known binary and recoil lobe structure, the cross sections show additional, smaller maxima for electron emission out of the projectile scattering plane. This observation, and the recently published cross sections at high impact energy [28], are consistent with the results of previous experiments by Schulz *et al* for ion impact [21, 22]. This indicates that their results were not purely due to instrumental effects as suggested in [26]. There is no theoretical model presently available, which quantitatively reproduces the ion-impact data out of the scattering plane. The situation for electron impact at $E_0 = 102$ eV is different, since we present several theories whose predictions are in good agreement with the experimental findings in the perpendicular plane geometry. The CCC model, applied with the neglect of exchange between the two active electrons, and with the passive second target electron considered within the frozen core model, yields generally very good agreement with the experimental data in and out of the scattering plane. The DWB2-CM model also reproduces the out-of-plane structure very well, but it overestimates the in-plane binary and recoil peaks for large momentum transfers. This is probably due to the increased importance of higher order effects, which are neglected in the second-order treatments. The DWB2-B model also yields significant out-of-plane electron emission, but generally the predicted second-order effects are smaller than those seen in the DWB2-CM approach. Finally, the 3C model nicely reproduces the cross section within the scattering plane, including the angular positions and relative heights of the binary and recoil peaks. On the other hand, it fails completely in describing the secondary peaks in the out-of-plane geometry. It was argued [25] that the underlying reason is the lack of accuracy of the 3C wavefunction when all three particles are close together, i.e., this model does not describe the projectile–nucleus scattering process properly.

In the future we plan to examine how the theories fare for $E_0 = 1$ keV electron impact [28], where the strength of the projectile–target interaction is close to that for fast ion impact (100 MeV/u C^{6+}) ionization of helium in the experiment performed by Schulz *et al* [21]. As mentioned above, so far all theories have failed to quantitatively reproduce the experimental ion-impact results. It will be interesting to see whether the case of electron-impact ionization of simple atoms is, indeed, better understood theoretically.

Acknowledgments

MD would like to thank M Schulz for helpful assistance with the generation of three-dimensional cross section images. CD acknowledges support from the EU within the HITRAP project (HPRI-CT-2001-50036). IB and DVF are grateful to the Australian Research Council and to ISA Technologies, Perth, Western Australia, for providing access to their IBM P690 computer in support of this project. Finally, this project was supported by the United States National Science Foundation under grants PHY-0456528 (ZC and DHM) and PHY-0244470 (KB).

References

[1] Ehrhardt H, Schulz M, Tekaat T and Willmann K 1969 *Phys. Rev. Lett.* **22** 89
[2] Lahmam–Bennani A 1991 *J. Phys. B: At. Mol. Opt. Phys.* **24** 2401–42

[3] Berakdar J 1996 *Phys. Rev.* A **53** 2314
[4] Jones S, Madison D and Konovalov D 1997 *Phys. Rev.* A **55** 444
[5] Jones S and Madison D 2000 *Phys. Rev.* A **62** 042701
[6] Brauner M, Briggs J S and Klar H 1989 *J. Phys. B: At. Mol. Opt. Phys.* **22** 2265–87
[7] Reid R H G, Bartschat K and Raeker A 1998 *J. Phys. B: At. Mol. Opt. Phys.* **31** 563–71
[8] Fang Y and Bartschat K 2001 *J. Phys. B: At. Mol. Opt. Phys.* **34** L19–25
[9] Bellm S, Lower J and Bartschat K 2006 *Phys. Rev. Lett.* **96** 223201
[10] Chen Z, Madison D H, Whelan C T and Walters H R 2004 *J. Phys. B: At. Mol. Opt. Phys.* **37** 981–95
[11] Chen Z and Madison D H 2005 *J. Phys. B: At. Mol. Opt. Phys.* **38** 4195–209
[12] Rescigno T N, Baertschy M, Isaacs W A and McCurdy C W 1999 *Science* **286** 2474–9
[13] Bray I 2002 *Phys. Rev. Lett.* **89** 273201
[14] Colgan J, Pindzola M S, Robicheaux F J, Griffin D C and Baertschy M 2002 *Phys. Rev.* A **65** 042721
[15] Horner D A, McCurdy C W and Rescigno T N 2005 *Phys. Rev.* A **71** 010701
[16] Horner D A, McCurdy C W and Rescigno T N 2005 *Phys. Rev.* A **71** 012701
[17] Bray I and Fursa D V 1996 *Phys. Rev. Lett.* **76** 2674–7
[18] Bray I and Fursa D V 1996 *Phys. Rev.* A **54** 2991–3004
[19] Stelbovics A T, Bray I, Fursa D V and Bartschat K 2005 *Phys. Rev.* A **71** 052716
[20] Colgan J, Pindzola M S, Childers G and Khakoo M A 2006 *Phys. Rev.* A **73** 042710
[21] Schulz M, Moshammer R, Fischer D, Kollmus H, Madison D H, Jones S and Ullrich J 2003 *Nature (London)* **422** 48–50
[22] Schulz M, Moshammer R, Fischer D and Ullrich J 2003 *J. Phys. B: At. Mol. Opt. Phys.* **36** L311–7
[23] Voitkiv A B, Najjari B and Ullrich J 2003 *J. Phys. B: At. Mol. Opt. Phys.* **36** 2591–609
[24] Olson R E and Fiol J 2003 *J. Phys. B: At. Mol. Opt. Phys.* **36** L365–73
[25] Madison D H, Fischer D, Foster M, Moshammer R, Jones S and Ullrich J 2003 *Phys. Rev. Lett.* **91** 253201
[26] Fiol J, Otranto S and Olson R E 2006 *J. Phys. B: At. Mol. Opt. Phys.* **39** L285–90
[27] Fischer D, Moshammer R, Schulz M, Voitkiv A and Ullrich J 2003 *J. Phys. B: At. Mol. Opt. Phys.* **36** 3555–67
[28] Dürr M, Dimopoulou C, Najjari B, Dorn A and Ullrich J 2006 *Phys. Rev. Lett.* **96** 243202
[29] Röder J, Ehrhardt H, Bray I, Fursa D V and McCarthy I E 1996 *J. Phys. B: At. Mol. Opt. Phys.* **29** 2103–14
[30] Murray A J, Woolf M B and Read F H 1992 *J. Phys. B: At. Mol. Opt. Phys.* **25** 3021–36
[31] Murray A J and Read F H 1992 *Phys. Rev. Lett.* **69** 2912–4
[32] Murray A J, Bowring N J and Read F H 2000 *J. Phys. B: At. Mol. Opt. Phys.* **33** 2859–67
[33] Rösel T, Röder J, Frost L, Jung K, Ehrhardt H, Jones S and Madison D H 1992 *Phys. Rev.* A **46** 2539–52
[34] Beaty E C, Kesselbacher K H, Hong S P and Moore J H 1978 *Phys. Rev.* A **17** 1592–9
[35] Ullrich J, Moshammer R, Dorn A, Schmidt L P and Schmidt-Böcking H 2003 *Rep. Prog. Phys.* **66** 1463–545
[36] Jagutzki O *et al* 2002 *IEEE Trans. Nucl. Sci.* **49** 2477–83
[37] Dorn A, Kheifets A, Schröter C D, Najjari B, Höhr C, Moshammer R and Ullrich J 2002 *Phys. Rev.* A **65** 032709
[38] Schröter C D, Rudenko A, Dorn A, Moshammer R and Ullrich J 2005 *Nucl. Instrum. Methods* A **536** 312–8
[39] Tavard C and Najjari B 1996 *Int. J. Quantum Chem.* **60** 657
[40] Kheifets A, Bray I and Bartschat K 1999 *J. Phys. B: At. Mol. Opt. Phys.* **32** L433–8
[41] Fursa D V and Bray I 1995 *Phys. Rev.* A **52** 1279–98
[42] Bray I and Fursa D V 1996 *Phys. Rev.* A **54** 2991–3004
[43] Fursa D V and Bray I 2003 *J. Phys. B: At. Mol. Opt. Phys.* **36** 1663
[44] Hasan A, Maydanyuk N V, Fendler B, Voitkiv A, Najjari B and Schulz M 2004 *J. Phys. B: At. Mol. Opt. Phys.* **37** 1923–30
[45] Ehrhardt H, Jung K, Klar H, Lahmam-Bennani A and Schlemmer P 1987 *J. Phys. B: At. Mol. Phys.* **20** L193–6